

1           **High-resolution Beijing MST radar detection of tropopause structure and**  
2                           **variability over Xianghe (39.75° N, 116.96° E), China**

3           Feilong Chen<sup>1</sup>, Gang Chen<sup>1\*</sup>, Yufang Tian<sup>2</sup>, Shaodong Zhang<sup>1</sup>, Kaiming Huang<sup>1</sup>,  
4   Chen Wu<sup>1</sup>, Weifan Zhang<sup>1</sup>

5           <sup>1</sup>School of Electronic Information, Wuhan University, Wuhan 430072, China.

6           <sup>2</sup>Key Laboratory of Middle Atmosphere and Global Environment Observation, Institute  
7           of Atmospheric Physics, Chinese Academy of Sciences, Beijing 100029, China.

8           \*Corresponding author: Gang Chen (g.chen@whu.edu.cn)

9  
10          **Abstract.**

11          As a result of partial specular reflection from the atmospheric stable layer, the radar  
12          tropopause (RT) can simply and directly be detected by VHF radars with vertical  
13          incidence. Here, the Beijing MST radar measurements are used to investigate the  
14          structure and the variabilities of the tropopause in Xianghe, China with a temporal  
15          resolution of 0.5 hour from November 2011 to May 2017. High-resolution radar-  
16          derived tropopause is compared with the thermal lapse-rate tropopause (LRT) that  
17          defined by the World Meteorological Organization (WMO) criterion from twice daily  
18          radiosonde soundings and with the dynamical potential vorticity tropopause (PVT) that  
19          defined as the height of 2 PVU surface. During all the seasons, the RT and the LRT in  
20          altitude agree well with each other with a correlation coefficient of  $\geq 0.74$ . Statistically,  
21          weaker (higher) tropopause sharpness seems to contribute to larger (smaller) difference  
22          between the RT and the LRT in altitude. The RT agrees well with the PVT in altitude  
23          during winter and spring with a correlation coefficient of  $\geq 0.72$ , while the correlation

24 coefficient in summer is only 0.33. As expected, the monthly mean RT and LRT height  
25 both show seasonal variations. Lomb-Scargle periodograms show that the tropopause  
26 exhibits obvious diurnal variation throughout the seasons, whereas the semidiurnal  
27 oscillations are rare and occasionally observed during summer and later spring. Our  
28 study shows the potential of the Beijing MST radar to determine the tropopause height,  
29 as well as present its diurnal oscillations.

30 **Key words:** VHF radar; MST radar; tropopause; diurnal oscillation.

31

## 32 **1. Introduction**

33 The tropopause marks a transition zone separating the well-mixed convectively  
34 active troposphere from the stably stratified and more quiescent stratosphere. Its  
35 structure and variability is characterized by large changes in thermal (e.g., lapse rate),  
36 dynamical (e.g., potential vorticity), and chemical properties (e.g., ozone and water  
37 vapor) and hence acts as a key role for the stratosphere-troposphere exchange (STE)  
38 processes (Hoinka, 1998; Seidel et al., 2001). The height of the tropopause depends  
39 significantly on the latitude, with about 17 km near the equator and less than 9-10 km  
40 at polar latitudes (Ramakrishnan, 1933). Over subtropical latitudes with the presence  
41 of subtropical jet, where the tropopause experiences rapid change or breaking,  
42 tropopause folding events are commonly observed (Pan et al., 2004). Climatologically,  
43 the altitude of the tropopause represents the seasonal variation of the flux of  
44 stratospheric air intruding into the troposphere (Appenzeller et al., 1996). Moreover,  
45 the tropopause height trends can be a sensitive indicator of anthropogenic climate

46 change (Sausen and Santer, 2003; Santer et al., 2003a; Añel et al., 2006).

47 A variety of ways are available to determine the extratropical tropopause.  
48 Radiosonde sounding is the most commonly used to define the thermal tropopause  
49 (hereafter referred to as LRT) based on temperature lapse-rate (WMO, 1957). The  
50 thermal definition of tropopause can be applied globally and the tropopause height  
51 easily be determined from one individual profile (Santer et al., 2003). Another feasible  
52 definition is to use a specific potential vorticity (PV) surface to represent the dynamical  
53 tropopause (hereafter referred to as PVT) (Reed, 1955; Hoskins et al., 1985).  
54 Dynamical definition has the advantage that the PV is a conserved property (under  
55 adiabatic and friction-less conditions) of an air mass (Hoskins et al., 1985; Bethan et  
56 al., 1996). Values in the range 1-4 PVU ( $1 \text{ PVU} = 10^6 \text{ m}^2 \text{ s}^{-1} \text{ K kg}^{-1}$ ) are used in previous  
57 researches in the Northern Hemisphere (e.g. Baray et al., 2000; Sprenger et al., 2003;  
58 Hoerling et al., 1991). The threshold of 2 PVU surface is the most commonly used  
59 (Gettelman et al., 2011). Dynamical definition, however, is not applicable near the  
60 equator, where the PV tends to be 0 (e.g., Hoerling et al., 1991; Nielsen-Gammon et al.,  
61 2001). Creating a blended tropopause globally may probably a good way forward  
62 (Wilcox et al., 2011). In addition, the data of GPS radio occultation satellites is also an  
63 effective way and commonly applied to study tropopause (e.g. Schmidt et al., 2005;  
64 Son et al., 2011).

65 As a result of partial specular reflection from stable atmospheric layer, the radar  
66 tropopause (RT) can be well represented and identified by atmospheric radars operating  
67 at meter wavelength (VHF band) and directing at vertical incidence (Gage and Green,

68 1979). Research activity increased remarkably following the first report on VHF radar  
69 detection of tropopause by Gage and Green (1979), for instance, the researches in  
70 middle latitudes (e.g. Hermawan et al., 1998), polar regions (e.g. Hall, 2013a), and  
71 tropical regions (e.g. Das et al., 2008; Ravindrababu et al., 2014). Several methods have  
72 been proposed to determine the tropopause height via radar echo power, including the  
73 largest gradient in echo power (Vaughan et al., 1995; Alexander et al., 2013), the  
74 maximum echo power (Vaughan et al., 1995; Hall et al., 2009), and the specific value  
75 of echo power (Gage and Green, 1982; Yamamoto et al., 2003). The method of the RT  
76 height determination used in this paper will be described in detail in next section.

77 The biggest advantage of the VHF radar measurements is the ability of continuous  
78 operation unmanned in any weather conditions. Of course, no definition of the  
79 tropopause is perfect. VHF radar system can only be limited to a few locations globally.  
80 A detailed review of the close relationship between these different tropopause  
81 definitions is provided by Alexander et al., (2012).

82 By means of the radiosonde, reanalysis, and satellite data available globally, long-  
83 term (annual or longer) variability in tropopause height has received extensive attention  
84 (e.g. Randel et al., 2000; Angell and Korshover, 2009; Son et al., 2011; Liu et al., 2014).  
85 However, short period (diurnal or semidiurnal) variability of the tropopause is hard to  
86 be examined by these measurements. In contrast, benefiting from the much higher  
87 temporal resolution, radar definition of the tropopause provides good capability for  
88 studying the diurnal and semidiurnal variation in tropopause height. Earlier, Yamamoto  
89 et al., (2003) reported the capability of the Equatorial Atmospheric Radar to examine

90 the diurnal variation of tropopause height. Then, the diurnal variability of the tropical  
91 tropopause was investigated in detail by Das et al., (2008) using the Indian Gadanki  
92 MST radar. Its diurnal variation over a polar latitude station was investigated by Hall  
93 (2013b). In the absence of pressure and temperature parameters, the evidence of  
94 atmospheric tides can be well represented by winds (e.g. Huang et al., 2015).

95 The tropopause structure in midlatitudes is different from that in other regions.  
96 Double tropopauses structure is a ubiquitous feature over mid-latitude regions near  
97 40°N (Pan et al., 2004; Randel et al., 2007). Strong evidence has revealed that the  
98 poleward intrusion of subtropical tropospheric air that occurred above the subtropical  
99 jet have resulted in the double structure (Pan et al., 2009). The higher part (second  
100 tropopause near ~16 km) is characterized by tropical features of cold and higher level,  
101 whereas the lower part (first tropopause near ~12 km) is characterized by polar features  
102 of warm and lower level. In the present study, we focus only on the first tropopause  
103 (below 16 km, if it exists) which will be referred to as ‘tropopause’ hereafter.

104 In this study, using more than 5 years of Beijing MST radar echo power  
105 measurements in vertical beam, we mainly focus on the high-resolution characteristics  
106 of the tropopause structure and their comparison with the simultaneous radiosonde and  
107 dynamical definitions. Another important objective of this study is to examine the  
108 diurnal and semidiurnal variability of the tropopause. The observational characteristics  
109 of e.g. winds, echo power, and data acquisition rate near the tropopause layer are also  
110 presented in the paper.

111

## 112 **2. Data and Methods**

### 113 **2.1. Radar Dataset**

114 As an important part of the Chinese Meridian Project, two MST radar systems are  
115 designed and constructed to improve the understanding of the extratropical troposphere,  
116 lower stratosphere, and mesosphere (Wang, 2010), which are Wuhan and Beijing MST  
117 radars. The Beijing MST radar located in Xianghe, Hebei Province, China ( $39.75^\circ$  N,  
118  $116.96^\circ$  E, 22 m above sea level) was designed and constructed by the Institute of  
119 Atmospheric Physics, Chinese Academy of Sciences and started its routine operation  
120 since 20 October 2011 (Tian and Lu, 2017). The radar is a high power coherent pulse-  
121 Doppler radar operating at 50 MHz with the maximum peak power of 172 kW and the  
122 half-power beam width of  $3.2^\circ$ . Five beams are applied: one vertically pointed beam  
123 and four  $15^\circ$  off-zenith beams tilted to north, east, south, and west. In order to obtain  
124 the high-quality measurements from troposphere, lower stratosphere, and mesosphere  
125 simultaneously, the radar is designed to operate routinely in three separate modes: low  
126 mode (designed range 2.5~12 km), middle mode (10~25 km), and high mode (60~90  
127 km) with vertical resolutions of 150, 600, and 1200 m, respectively. Under the routine  
128 operation, the 15-min break is followed by the 15-min operation cycle (5 min for each  
129 mode). As a result, the time resolutions of the low, middle, and high mode  
130 measurements are all 30 min. More detailed review of the radar system is given by  
131 Chen et al. (2016).

132 Here only the low mode echo power measurements are used to determine the RT  
133 height. Although the designed detectable range of the low mode is from 2.5~12 km,

134 the vertically pointed beam can receive stronger echoes from a higher level (~14-15 km)  
135 as compared with those from off-vertical beams due to the partial specular reflection  
136 mechanism. The measurements in middle mode are also applied to calculate the winds  
137 or echo power within ~5-6 km of the tropopause. The parameters for the two routine  
138 operation modes are listed in Table 1. The monthly total number of the echo power  
139 profiles available in vertical beam (low mode) is shown in Fig. 1. The outliers or  
140 severely contaminated data that mainly induced by system problems are eliminated.  
141 The large data gap in September is due to the annual preventive maintenance.

## 142 **2.2. Tropopause Definitions**

143 Due to the large gradient in potential temperature, radar return power received at  
144 vertical incidence is significantly enhanced upon the transition zone of the tropopause  
145 layer. Using this characteristic, the RT height can be determined effectively by the VHF  
146 radar. Here, the RT is defined as the altitude (above 500 hPa) where the maximum  
147 vertical gradient of echo power is located (Vaughan et al., 1995; Alexander et al.,  
148 2013; Ravindrababu et al., 2014; Chen et al., 2018). Considering the occasional and  
149 random noise, to which the derived-RT is sensitive, the echo power profiles are  
150 smoothed by a 3-point running mean. In order to further reduce the influence of the  
151 noise, the RT definition used here need to satisfy an additional criterion: the determined  
152 RT height should be continuous with the adjacent RT heights (one on each side),  
153 otherwise to search for the second peak gradient (eliminated if the second peak does  
154 not meet the additional criterion). The “continuous” here means that the discrepancy  
155 between the two successive heights (in time, 0.5-hour interval) should be <0.6 km. A

156 typical example of the RT and LRT is illustrated in Fig. 2. The LRT is identified based  
 157 on the World Meteorological Organization (WMO) criteria (WMO, 1957). The radar  
 158 aspect sensitivity is expressed as the ratio between vertical ( $p_v$ ) and oblique ( $p_o$ ) beam  
 159 echo power (here is  $15^\circ$  east beam). The radiosonde soundings are launched twice daily  
 160 from the Beijing Meteorological Observatory ( $39.93^\circ\text{N}$ ,  $116.28^\circ\text{E}$ , station number  
 161 54511), which is less than 45 km to the radar site. In this case, the LRT and RT  
 162 consistent well and are at 11.65 km and 11.85 km respectively. As expected, the LRT  
 163 characterized by a rapid increase in potential temperature gradient also corresponds to  
 164 the large gradient in radar aspect sensitivity. Note that the height with maximum value  
 165 in echo power lie at a higher altitude (as compared with the RT height) of  $\sim 700$  m above  
 166 the LRT. The dynamical tropopauses used in this paper are derived from the European  
 167 Centre for Medium-Range Weather Forecasts (ECMWF) ERA-Interim Reanalysis (Dee  
 168 et al., 2011) and defined as the surface of 2 PVU potential vorticity, which is same to  
 169 that used by Sprenger et al., (2003) and Alexander et al. (2013).

### 170 **2.3. Tropopause sharpness definition**

171 For the compared data pairs between the RT and LRT, we calculate the  
 172 corresponding tropopause sharpness that represents the strength of the tropopause  
 173 inversion layer. As defined by Wirth, (2000), the tropopause sharpness  $S_{TP}$  can be  
 174 calculated as:

$$175 \quad S_{TP} = \frac{T_{TP+\Delta Z} - T_{TP}}{\Delta Z} - \frac{T_{TP} - T_{TP-\Delta Z}}{\Delta Z} \quad (1)$$

176 where TP denotes the tropopause height,  $\Delta Z = 1$  km, and  $T_{TP}$  indicates the

177 corresponding temperature. This definition is also used in Alexander et al. 2013 and  
178 we're using it for a good comparison with our results.

### 179 **3. Results**

#### 180 **3.1. High-resolution radar tropopause structure**

181 The height-time cross section of radar echo power and aspect sensitivity is shown  
182 in Fig. 3 for a typical month (February 2014), along with the RT, PVT and LRT marked  
183 in the figure. In general, the RT agreed well with both the LRT and PVT in height, and  
184 most of the RT exhibit a slightly higher altitude. However, the differences between the  
185 RT and LRT are sometimes large (reach to ~1-2 km) especially when the RT experience  
186 rapid change. Regardless of the background synoptic condition, the difference in the  
187 definitions themselves is to a large degree the main contributing factor for the large  
188 difference between the RT and LRT. For example, a second layer with significant  
189 enhanced echo power is observed above the radar-derived RT for the cases on 4 and 5  
190 February 2012 (Fig.3a). According to the definitions, the RT is well defined as the first  
191 layer with enhanced echo power and the LRT matched the second layer, similar to that  
192 observed by Yamamoto et al., (2003) and Fukao et al., (2003). It is of note that the RT  
193 well separates the troposphere characterized by low aspect sensitivity from the lower-  
194 stratosphere characterized by high aspect sensitivity (Fig.3b).

#### 195 **3.2. Comparisons between different definitions**

196 To further quantify the consistency and difference in altitude between different  
197 tropopause definitions, a detailed comparison is carried out in this section. The seasonal  
198 scatterplots for RT versus LRT and the histogram distribution of altitude differences

199 between the RT and LRT are illustrated in Fig. 4, during the period November 2011-  
200 May 2017. A total of 2411 data pairs are obtained for comparison. Among them, the  
201 number of data pairs is 845 for DJF (winter), 721 for MAM (spring), 321 for JJA  
202 (summer), and 524 for SON (autumn). Comparisons have shown a good consistency  
203 throughout the seasons and most of the RTs exhibit a slightly higher than the LRTs. The  
204 correlation coefficient is 0.74, 0.80, 0.82, and 0.78 for DJF, MAM, JJA, and SON,  
205 respectively. The mean and standard deviation difference (RT minus LRT) calculated  
206 in DJF, MAM, JJA, and SON is  $(0.14 \pm 0.75)$ ,  $(0.26 \pm 0.78)$ ,  $(0.33 \pm 0.56)$ , and  
207  $(0.12 \pm 0.69)$  km, respectively. The proportion of the data pairs with differences  $<500$  m  
208 is reasonably good during four seasons and is 63%, 61%, 64%, and 67% for DJF, MAM,  
209 JJA, and SON, respectively. Fig. 4 explicitly shows that the RT derived by the Beijing  
210 MST radar agrees reasonably well with the LRT throughout the seasons.

211 To examine the potential role of the sharpness, Fig. 5a and Fig. 5b show the  
212 histogram distribution of the tropopause sharpness along with the probability density  
213 curve for data pairs with difference (absolute values of RT minus LRT)  $<0.5$  km and  $>1$   
214 km respectively. What is apparent is that most data pairs of Fig. 5a are located to the  
215 right (higher sharpness values, with the peak of  $\sim 7.06$  K/km) and of Fig. 5b are to the  
216 left (lower sharpness values, with the peak of  $\sim 6.35$  K/km). No matter whether this  
217 distribution feature is associated with the cyclonic-anticyclonic systems (e.g. Randel et  
218 al., 2007; Randel and Wu, 2010), the results more or less demonstrate that the larger  
219 (weaker) tropopause sharpness contribute to lower (higher) difference between the RT  
220 and LRT. From the perspective of seasonal statistics, the tropopause sharpness over

221 Beijing station shows similar distribution characteristics throughout the seasons (not  
222 shown), which is different from that in polar regions where the sharpness is significantly  
223 higher during summer than during winter (Zänagl and Hoinka, 2001).

224 The seasonal scatterplots and height difference distribution between the RT and  
225 PVT are illustrated and quantified in Fig. 6. The total number of comparing data pairs  
226 for winter, spring, summer, and autumn is 1422, 1260, 791, and 1145, respectively.  
227 During winter and spring (Fig. 6a and 6b), the RTs agree reasonably well with the PVTs  
228 with the correlation coefficient of 0.72 and 0.76 and the mean difference (RT minus  
229 PVT) of  $(0.55 \pm 0.84 \text{ km})$  and  $(1 \pm 0.89 \text{ km})$ , respectively. In contrast, the consistency  
230 for summer and autumn (Fig. 6c and 6d) is relatively bad and with correlation  
231 coefficient of 0.33 and 0.47 and mean difference of  $(0.80 \pm 1.39 \text{ km})$  and  $(0.75 \pm 1.23$   
232  $\text{ km})$ , respectively. Especially for summer, the proportion of the comparing data pairs  
233 with difference  $<0.5 \text{ km}$  is only 10.6% (84). In autumn, need to note that most data pairs  
234 with poor consistency is sampled during early autumn.

### 235 **3.3. Observational characteristics in the vicinity of tropopause**

236 Measurements of radar middle mode are used for examining the horizontal wind,  
237 return power, and effective wind data acquisition rate within 5-6 km of the tropopause  
238 (upper troposphere and lower stratosphere). Left panels of Fig. 7 show the vertical  
239 scatterplots of the static stability (represented by the buoyancy frequency squared) as a  
240 function of height relative to the LRT and the right panels show the radar echo power  
241 as a function of height relative to the RT, during two specific years 2012-2013 for  
242 extended winter NDJFM and summer MJJAS seasons. Mean and standard deviations

243 are also plotted in each panel of Fig. 7. As expected, results clearly show sudden jump  
244 in static stability and radar power near the tropopause layer. The degree of sudden  
245 increase in echo power is more gradual than that in static stability. The amplitude of the  
246 sudden increase in radar power experienced a slightly larger during NDJFM than that  
247 during MJJAS (red lines of right panels). Another interesting feature in the lower-  
248 stratosphere is that both the static stability and radar power points show less disperse  
249 during NDJFM than that during MJJAS.

250 Fig. 8 shows the profiles of mean radar effective wind data acquisition rate for low  
251 and middle modes during November 2011-May 2017. Clearly, both profiles exhibit a  
252 sudden increase with height near the tropopause, with the first peak located  $\sim 1$  km  
253 higher above the mean tropopause height. Note that the second inversion in middle  
254 mode profile that occurred near 16 km is associated with the second tropopause. As  
255 limited by the highest detectable altitude (the data acquisition rate decreased to lower  
256 than 20% at  $\sim 16$  km), the profile in low mode shows little evidence of second inversion.

257 Fig. 9 shows time-height intensity plot of the monthly mean radar-derived  
258 horizontal wind (from middle mode) during November 2011-May 2017, together with  
259 the monthly mean location of RT and LRT. One pixel grid denotes 1 month $\times$ 0.6 km.  
260 The monthly mean RT and LRT agreed well with each other in height, within 400 m in  
261 August and September and even lower in other months of about within 200 m. They  
262 both exhibit a clear seasonal variation, with maximum in early autumn of  $\sim 11.6$  km and  
263 minimum in early spring of  $\sim 10.3$  km. The monthly mean wind jet varies with season,  
264 with the thinnest thickness and lowest strength in summer. The mean tropopause height

265 appears to correspond to the lower boundary location of peak wind layer. The error bars  
266 of both the RT and LRT help to illustrate that the tropopauses changes by larger  
267 amplitude in winter and June than that in other months.

### 268 **3.4. Periodogram analysis of the radar tropopause**

269 High temporal resolution detection of tropopause by VHF radar have allowed us  
270 to investigate the diurnal or semidiurnal variability of the tropopause. Atmospheric tides  
271 are well known global oscillations contributing to the diurnal variation in temperature  
272 and background winds, which in turn modulate the tropopause height. With the absence  
273 of temperature measurements, zonal and meridional winds are applied to demonstrate  
274 the evidence of diurnal or semidiurnal modulation by tidal. The frequency power  
275 spectrum of the RT height, zonal and meridional wind, calculated by means of Lomb-  
276 Scargle method (Press and Rybicki, 1989), is illustrated in Fig. 10 for two typical  
277 months: May 2015 and December 2016. The choice of Lomb-Scargle algorithm is due  
278 to the presence of data gaps ( $\sim 2$  days per week, especially during 2012-2013). The  
279 dominant  $\sim 24$  h periodicity in RT height, zonal and meridional wind is obvious for both  
280 months. The evidence of  $\sim 12$  h period in all three parameters is distinct for May 2015  
281 (Fig. 10a), although the power is relatively weaker. Through the analysis for each  
282 individual month, we found that the semidiurnal component in the three parameters is  
283 generally and occasionally observed in summer and later spring during our  
284 experimental period. The characteristics of the diurnal variation of the RT height can  
285 be represented better in Fig. 11, which shows the mean Lomb-Scargle power spectrum  
286 of the RT as a function month during November 2011-May 2017. As compared with

287 other months, the dominant diurnal periodicity is less evident in April. We need to  
288 clarify that atmospheric tides are of course not the only source of the diurnal variation  
289 in tropopause height, diurnal convective activities (Yamamoto et al., 2003) might also  
290 be an important cause. Here will not be discussed in detail.

291

#### 292 **4. Discussion**

293 As for the radar echo power definition, the RT estimation sometimes will fail due  
294 to the system problems, even if the thermal tropopause is well defined (Hall et al., 2009).  
295 Apart from the system problems (e.g. the damage of T/R module), the following two  
296 conditions are primarily responsible for the failure (or difficulty) of both the radar and  
297 thermal definitions over the radar site latitude ( $\sim 40^\circ$  N). Firstly, the temperature  
298 sometimes continued to decrease until to the stratosphere (above 16 km) in summer and  
299 early autumn, leading to the failure/difficulty of both the radar and thermal definitions  
300 (a typical case as shown in Fig. 12a). Need to note that the temperature inversion layer  
301 occurred at  $\sim 16$  km in summer or early autumn is the second tropopause with  
302 characteristics of Tropics (Pan et al., 2004; Randel et al., 2007). Secondly, some specific  
303 meteorological processes can lead to the ambiguities and indefiniteness in thermal and  
304 radar definitions, such as fronts, cyclones or typhoons, and folding (e.g. Nastrom et al.,  
305 1989; May et al., 1991; Roettger, 2001; Alexander et al., 2013). Such ambiguities often  
306 result in large difference in altitude between the RT and LRT. In addition, when multiple  
307 temperature inversion layers occurred (below 16 km), the RT sometimes matched the  
308 lower layer with enhanced echo power and LRT often matched the upper layer (e.g.

309 Yamamoto et al., 2003; Fukao et al., 2003). Apart from the situations above, another  
310 condition is also commonly responsible for the difficult in identifying the thermal  
311 tropopause from radiosonde profiles during summer. As a typical case shown in Fig.  
312 12b, a significant inversion in temperature (at ~12 km) is recorded from the radiosonde  
313 profile, but the altitude extent of inversion layer is too thin to meet the WMO criterion  
314 that thermal definition required. Whereas, the apparent enhancement in radar echo  
315 power corresponding to such inversion layer is strong enough to well define the RT.  
316 The temperature inversion located near ~16 km (the second tropopause) is not the focus  
317 of this paper.

318 Pan et al., (2004) have reported that the difference between the LRT and PVT are  
319 more distinct in the vicinity of subtropical jet. In the northern hemisphere, the axis of  
320 the subtropical jet is situated near ~30°N in spring and winter, whereas in summer and  
321 early autumn the subtropical jet shifts northward to ~40°N (see Fig. 4 in Ding and Wang,  
322 2006). We preliminary considered that the inconsistency between the RT and PVT in  
323 summer and early autumn (Fig. 6c and 6d) is most likely related to the subtropical jet  
324 shifting poleward to ~40°N. The existing cyclones or anticyclones in the upper-  
325 troposphere (Wirth, 2000), of course, may also be an important influence factor for the  
326 significant asymmetric differences (most of the scattered points deviate significantly  
327 from the 1:1 line). The asymmetric differences, that is most of the RT are located higher  
328 than the 2PVU tropopause height, suggest that the 2PVU surface is not the best measure  
329 of a dynamical tropopause over Beijing during summer-time. More detailed discussion  
330 about the striking asymmetric differences in height between LRT and PVT can be seen

331 in Wirth (2001) and will not be given here. Anyway, we need to be careful when using  
332 the 2PVU dynamical definition to define the tropopause over radar site latitude  $\sim 40^\circ$  N,  
333 especially in summer.

334 About the characteristics of tropopause and the comparison between different  
335 definitions, there are many differences between mid-latitude and polar regions. In mid-  
336 latitude ( $\sim 40^\circ$ N), our results show that: (1) the agreement between RT and LRT is  
337 similar good throughout the seasons; (2) RTs are generally located higher than the LRT;  
338 (3) the thermal definition sometimes fail in summer and early autumn; (4) the  
339 agreement between the RT/LRT and PVT in summer is poor. Whereas, in contrast,  
340 previous researches about the tropopause over polar regions reported that (Wirth, 2000;  
341 Alexander et al., 2013): (1) the difference between the RT and LRT is larger during  
342 winter than that during summer; (2) RTs are generally located lower than the LRT; (3)  
343 the thermal definition sometimes fail in winter and spring; (4) the comparison between  
344 the RT and PVT showed the similar good agreement during both summer and winter.

345 Over a polar latitude station, the seasonal characteristics of the diurnal oscillation  
346 in tropopause height were investigated using 5 years of SOUSY VHF radar  
347 measurements (Hall, 2013b). The sunlight variability in polar regions is different from  
348 that in other latitudes of the world. Different sunlight variation actually will lead to  
349 difference in atmospheric tides, and then would result in different diurnal variation in  
350 tropopause height. Here we found that the diurnal oscillation of RT height at Xianghe  
351 is ubiquitous and obvious throughout the seasons except for April (Fig. 11). Whereas at  
352 polar latitude and in months of November to February when there is no sunlight, Hall

353 (2013b) observed little evidence of 24 h diurnal variability in RT height.

354

## 355 **5. Conclusions**

356 In this paper, we present the high resolution structure and variability of the  
357 tropopause in Xianghe, China (39.75° N, 116.96° E), based on the Beijing MST radar  
358 vertical beam echo power data collected during the period November 2011-May 2017.  
359 Fine-scale structure of the RT is well determined with a high temporal resolution of 0.5  
360 h. Comparison results have shown good agreement in altitude between the RT and LRT,  
361 with a correlation coefficient of  $\geq 0.74$  for the four seasons. Higher tropopause  
362 sharpness seems to contribute lower difference between the RT and LRT in altitude and  
363 weaker sharpness appears responsible for higher difference. The agreement between  
364 the RT and PVT is relatively well in winter and spring with correlation coefficient of  
365 0.72 and 0.76 respectively, but poor during summer with a correlation coefficient of  
366 only 0.33. We initially suggested that the poor consistency between RT and PVT is  
367 associated with the subtropical jet shifting poleward to  $\sim 40^\circ\text{N}$ .

368 As expected, the sudden jump in static stability (represented by the buoyancy  
369 frequency squared) and the rapid increase in radar echo power upon the tropopause  
370 layer are clearly observed. Upon the tropopause layer, a sudden increase in effective  
371 radar data acquisition rate is also observed. Both the monthly mean RT and LRT height  
372 have shown a clear annual cycle. The variability and oscillation of RT height with  
373 diurnal or lower timescales is presented. Obvious diurnal variation in tropopause height,  
374 zonal wind, and meridional wind is generally observed throughout the seasons,

375 indicating the modulation most likely from the atmospheric tides. The semidiurnal  
376 variation in RT height is not so obvious and commonly observed occasionally in  
377 summer and late spring.

378

### 379 **Acknowledgment**

380 This work is funded by National Natural Science Foundation of China (NSFC grants  
381 No. 41474132 and 41722404). We acknowledge the Chinese Meridian Project for  
382 providing the MST radar data. The authors sincerely acknowledge the ECMWF for  
383 providing global reanalysis data. The MST radar data for this paper are available at  
384 Data Centre for Meridian Space Weather Monitoring Project (<http://159.226.22.74/>).  
385 The radiosonde data are publicly available from the NOAA/ESRL Database at  
386 <https://ruc.noaa.gov/raobs/>.

387

### 388 **References**

389 Alexander, S.P., Murphy, D.J., and Klekociuk, A.R.: High resolution VHF radar  
390 measurements of tropopause structure and variability at Davis, Antarctica (69° S,  
391 78° E), *Atmos. Chem. Phys.*, 13, 3121-3132, 2013.

392 Angell, J. K., and Korshover, J.: Quasi-biennial and long-term fluctuations in  
393 tropopause pressure and temperature, and the relation to stratospheric water vapor  
394 content. *Monthly Weather Review*, 102(1), 29-34, 2009.

395 Appenzeller, C., Holton, J. R., and Rosenlof, K. H.: Seasonal Variation of Mass  
396 Transport Across the Tropopause. *Journal of Geophysical Research*, 101(D10),

397 15071-15078, 1996.

398 Añel, J. A., J. C. Antuña, L. de la Torre, R. Nieto, and Gimeno L.: Changes in  
399 tropopause height for the Eurasian region determined from CARDS radiosonde  
400 data. *Naturwissenschaften*, 93, 603–609, doi:10.1007/s00114-006-0147-5, 2006.

401 Bethan, S., Vaughan, G., and Reid, S. J.: A comparison of ozone and thermal tropopause  
402 heights and the impact of tropopause definition on quantifying the ozone content  
403 of the troposphere. *Quarterly Journal of the Royal Meteorological Society*,  
404 122(532), 929-944, 1996.

405 Baray, J., Daniel, V., Ancellet, G., and Legras, B.: Planetary-scale tropopause folds in  
406 the southern subtropics. *Geophysical Research Letters*, 27(3), 353-356, 2000.

407 Chen, F. L., Chen, G., Shi, C. H., Tian, Y. F., Zhang, S. D., and Huang, K. M.: Strong  
408 downdrafts preceding rapid tropopause ascent and their potential to identify cross-  
409 tropopause stratospheric intrusions, *Annales Geophysicae*, 36(5), 1403-1417,  
410 2018.

411 Chen, G., Cui, X., Chen, F., Zhao, Z., Wang, Y., Yao, Q., and Gong, W.: MST Radars  
412 of Chinese Meridian Project: System Description and Atmospheric Wind  
413 Measurement. *IEEE Transactions on Geoscience and Remote Sensing*, 54(8),  
414 4513-4523, 2016.

415 Das, S. S., Jain, A. R., Kumar, K. K., and Rao, D. N.: Diurnal variability of the tropical  
416 tropopause: Significance of VHF radar measurements. *Radio Science*, 43(6), 1-14,  
417 doi:10.1029/2008RS003824, 2008.

418 Dee, D. P., Uppala, S. M., Simmons, A. J., Berrisford, P., Poli, P., Kobayashi, S. et al.:

419 The ERA-Interim reanalysis: configuration and performance of the data  
420 assimilation system. *Quarterly Journal of the Royal Meteorological Society*,  
421 137(656), 553-597, 2011.

422 Ding, A., and Wang, T.: Influence of stratosphere-to-troposphere exchange on the  
423 seasonal cycle of surface ozone at Mount Waliguan in western China. *Geophysical*  
424 *Research Letters*, 33(3), 233-252, doi:10.1029/2005GL024760, 2006.

425 Fukao, S., H. Hashiguchi, M. Yamamoto, T. Tsuda, T. Nakamura, M. K. Yamamoto,  
426 T. Sato, M. Hagio, and Y. Yabugaki.: Equatorial Atmosphere Radar (EAR):  
427 System description and first results. *Radio Science*, 38(3), 1053, 2003.

428 Gage, K. S., and Green, J. L.: An objective method for the determination of tropopause  
429 height from VHF radar observations. *Journal of Applied Meteorology*, 21(21),  
430 1150-1154, 1982.

431 Gage, K. S., and Green, J. L.: Tropopause Detection by Partial Specular Reflection with  
432 Very-High-Frequency Radar. *Science*, 203(4386), 1238-1240, 1979.

433 Gettelman, A., P. Hoor, L. L. Pan, W. J. Randel, M. I. Hegglin, and T. Birner: The  
434 extratropical upper troposphere and lower stratosphere, *Reviews of Geophysics*,  
435 49(3), RG3003, doi: 10.1029/2011RG000355, 2011.

436 Hermawan, E., Tsuda, T., and Adachi, T.: MU radar observations of tropopause  
437 variations by using clear air echo characteristics. *Earth, Planets and Space*, 50(4),  
438 361-370, 1998.

439 Hall, C.: The radar tropopause above Svalbard 2008–2012: Characteristics at various  
440 timescales. *Journal of Geophysical Research*, 118(6), 2600-2608, 2013a.

441 Hall, C.: The radar tropopause at 78°N, 16°E: Characteristics of diurnal variation.  
442 Journal of Geophysical Research, 118(12), 6354-6359, doi:10.1002/jgrd.50560,  
443 2013b.

444 Hall, C. M., Röttger, J., Kuyeng, K., Sigernes, F., Claes, S., and Chau, J. L.: Tropopause  
445 altitude detection at 78°N, 16°E, 2008: First results of the refurbished SOUSY  
446 radar. Radio Science, 44(5), 1-12, doi:10.1029/2009RS004144, 2009.

447 Hoinka, K. P.: Statistics of the Global Tropopause Pressure. Monthly Weather Review,  
448 126(12), 3303-3325, 1998.

449 Hoskins, B. J., McIntyre, M. E., and Robertson, A. W.: On the use and significance of  
450 isentropic potential vorticity maps. Quarterly Journal of the Royal Meteorological  
451 Society, 111(470), 877-946, 2007.

452 Huang, C., Zhang, S. D., Zhou, Q. H., Yi, F., Huang, K., Gong, Y., Zhang, Y., and Gan,  
453 Q.: WHU VHF radar observations of the diurnal tide and its variability in the lower  
454 atmosphere over Chongyang (114.14° E, 29.53° N), China. Annales Geophysicae,  
455 33(7), 865-874, 2015.

456 Hoerling, M. P., Schaack, T. K., and Lenzen, A. J.: Global Objective Tropopause  
457 Analysis. Monthly Weather Review, 119(8), 1816-1831, 1991.

458 Liu, Y., Xu, T., and Liu, J.: Characteristics of the seasonal variation of the global  
459 tropopause revealed by cosmic/GPS data. Advances in Space Research, 54(11),  
460 2274-2285, 2014.

461 May, P. T., Yamamoto, M., Fukao, S., Sato, T., Kato, S., and Tsuda, T.: Wind and  
462 reflectivity fields around fronts observed with a VHF radar. *Radio Science*, 26(5),  
463 1245-1249, 1991.

464 Nastrom, G. D., Green, J. L., Gage, K. S., and Peterson, M. R.: Tropopause Folding  
465 and the Variability of the Tropopause Height as Seen by the Flatland VHF Radar.  
466 *Journal of Applied Meteorology*, 28(12), 1271-1281, 1989.

467 Nielsen-Gammon, J. W.: A visualization of the global dynamic tropopause. *Bulletin of*  
468 *the American Meteorological Society*, 82(6), 1151-1168, 2001.

469 Pan, L. L., Randel, W. J., Gary, B. L., Mahoney, M. J., and Hints, E. J.: Definitions  
470 and sharpness of the extratropical tropopause: A trace gas perspective. *Journal of*  
471 *Geophysical Research*, 109, D23103, doi:10.1029/2004JD004982, 2004.

472 Pan, L. L., W. J. Randel, J. C. Gille, W. D. Hall, B. Nardi, S. Massie, V. Yudin, R.  
473 Khosravi, P. Konopka, and D. Tarasick: Tropospheric intrusions associated with  
474 the secondary tropopause, *Journal of Geophysical Research*, 114, D10302, 2009.

475 Press, W. H., and Rybicki, G. B.: Fast algorithm for spectral analysis of unevenly  
476 sampled data. *The Astrophysical Journal*, 338(1), 277-280, 1989.

477 Ravindrababu, S., Venkat Ratnam, M., Sunilkumar, S. V., Parameswaran, K., and  
478 Krishna Murthy, B. V.: Detection of tropopause altitude using Indian MST radar  
479 data and comparison with simultaneous radiosonde observations. *Journal of*  
480 *Atmospheric and Solar-Terrestrial Physics*, 121(6), 679-687, 2014.

481 Randel, W. J., Wu, F., and Gaffen, D. J.: Interannual variability of the tropical  
482 tropopause derived from radiosonde data and NCEP reanalyses. *Journal of*  
483 *Geophysical Research Atmospheres*, 105(D12), 15509-15523, 2000.

484 Randel, W. J., Seidel, D. J., and Pan, L. L.: Observational characteristics of double  
485 tropopauses. *Journal of Geophysical Research*, 112, D07309, 2007.

486 Randel, W. J., and Wu, F.: The Polar Summer Tropopause Inversion Layer. *Journal of*  
487 *the Atmospheric Sciences*, 67(8), 2572-2581, 2010.

488 Randel, W. J., Wu, F., and Forster, P. M.: The extratropical tropopause inversion layer:  
489 Global observations with GPS data, and a radiative forcing mechanism. *Journal of*  
490 *the Atmospheric Sciences*, 64(12), 4489-4496, 2007.

491 Ramakrishnan, K. P.: Distortion of the tropopause due to meridional movements in the  
492 sub-stratosphere. *Nature*, 132(3346), 932-932, 1933.

493 Roettger, J.: Observations of the polar d-region and the mesosphere with the Eiscat  
494 Svalbard radar and the SOUSY Svalbard Radar (scientific paper). *Memoirs of*  
495 *National Institute of Polar Research. Special Issue*, 54(94), 9-20, 2001.

496 Reed, R. J.: A study of a characteristic type of upper-level frontogenesis. *Journal of the*  
497 *Atmospheric Sciences*, 12(3), 226-237, 1955.

498 Santer, B. D., Wehner, M. F., Wigley, T. M., Sausen, R., Meehl, G. A., Taylor, K. E.,  
499 Ammann, C., Arblaster, J., Washington, W. M., Boyle, J. S., and Brüggemann, W.:  
500 Contributions of anthropogenic and natural forcing to recent tropopause height  
501 changes. *Science*, 301(5632), 479-483, 2003.

502 Santer, B. D., Sausen, R., Wigley, T. M., Boyle, J. S., Achutarao, K., Doutriaux, C.,

503 Hansen, J. E., Meehl, G. A., Roeckner, E., Ruedy, R., Schmidt, G., and Taylor, K.  
504 E.: Behavior of tropopause height and atmospheric temperature in models,  
505 reanalyses, and observations: Decadal changes. *Journal of Geophysical Research*,  
506 108(D1), 4002, doi:10.1029/2002JD002258, 2003a.

507 Sausen, R., and Santer, B. D.: Use of Changes in Tropopause Height to Detect Human  
508 Influences on Climate. *Meteorologische Zeitschrift*, 12(3), 131-136, 2003.

509 Schmidt, T., Heise, S., Wickert, J., Beyerle, G., & Reigber, C.: GPS radio occultation  
510 with CHAMP and SAC-C: global monitoring of thermal tropopause parameters.  
511 *Atmospheric Chemistry and Physics*, 5(6), 1473-1488, 2005.

512 Seidel, D. J., Ross, R. J., Angell, J. K., and Reid, G. C.: Climatological characteristics  
513 of the tropical tropopause as revealed by radiosondes. *Journal of Geophysical*  
514 *Research*, 106(D8), 7857-7878, 2001.

515 Son, S. W., Tandon, N. F., & Polvani, L. M.: The fine-scale structure of the global  
516 tropopause derived from COSMIC GPS radio occultation measurements. *Journal*  
517 *of Geophysical Research: Atmospheres*, 116(D20), 2011.

518 Sprenger, M., Croci Maspoli, M., and Wernli, H.: Tropopause folds and cross-  
519 tropopause exchange: a global investigation based upon ECMWF analyses for the  
520 time period March 2000 to February 2001. *Journal of Geophysical Research*  
521 *Atmospheres*, 108(12), 291-302, 2003.

522 Tian, Y., and Lu, D.: Comparison of Beijing MST Radar and Radiosonde Horizontal  
523 Wind Measurements. *Advances in Atmospheric Sciences*, 34(1), 39-53. doi:  
524 10.1007 / s00376-016-6129-4, 2017.

525 Vaughan, G., Howells, A., and Price, J. D.: Use of MST radars to probe the mesoscale  
526 structure of the tropopause. *Tellus A*, 47(5), 759-765, 1995.

527 Wang, C.: Development of the Chinese meridian project. *Chinese Journal of Space*  
528 *Science*, 30(4), 382–384, 2010.

529 Wilcox L.J., Hoskins B.J., Shine K.P. 2012. A global blended tropopause based on ERA  
530 data. Part I: Climatology. *Q. J. R. Meteorol. Soc.* 138: 561–575.  
531 DOI:10.1002/qj.951.

532 Wirth, V.: Thermal versus dynamical tropopause in upper-tropospheric balanced flow  
533 anomalies. *Quarterly Journal of the Royal Meteorological Society*, 126(562), 299-  
534 317, 2000.

535 Wirth, V.: Cyclone-anticyclone asymmetry concerning the height of the thermal and the  
536 dynamical tropopause. *Journal of the Atmospheric Sciences*, 58(1), 26-37, 2001.

537 WMO: Definition of the tropopause. *WMO Bull.*, 6, 136, 1957.

538 Yamamoto, M., Oyamatsu, M., Horinouchi, T., Hashiguchi, H., and Fukao, S.: High  
539 time resolution determination of the tropical tropopause by the Equatorial  
540 Atmosphere Radar. *Geophysical Research Letters*, 30(21), 2094, 2003.

541 Zängl, G., and Hoinka, K. P.: The tropopause in the polar regions. *Journal of Climate*,  
542 14(2001), 3117-3139, 2001.

543

544 **Table**

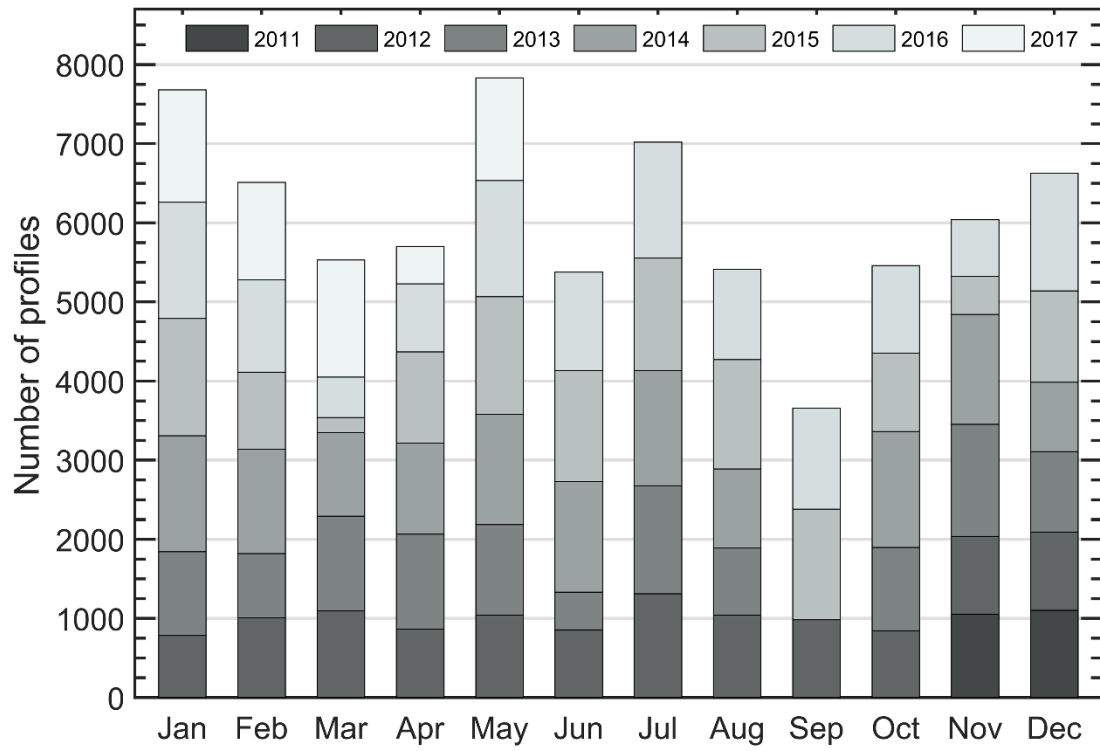
Radar parameter	Value
Transmitted frequency	50 MHz
Antenna array	24×24 3-element Yagi
Antenna gain	33 dB
Transmitter peak power	172 kW
Code	16-bit complementary
No. coherent integrations	128 (low mode)/64 (mid mode)
No. FFT points	256
No. spectral average	10
Pulse repetition period	160 (low mode)/320 (mid mode) $\mu$ s
Half power beam width	3.2°
Pulse length	1 (low mode)/4 (mid mode) $\mu$ s
Range resolution	150 (low mode)/600 (mid mode) m
Temporal resolution	30 min
Off-zenith angle	15°

545 **Table 1.** Routine operational parameters in low and middle mode for the Beijing MST

546 radar used in this study.

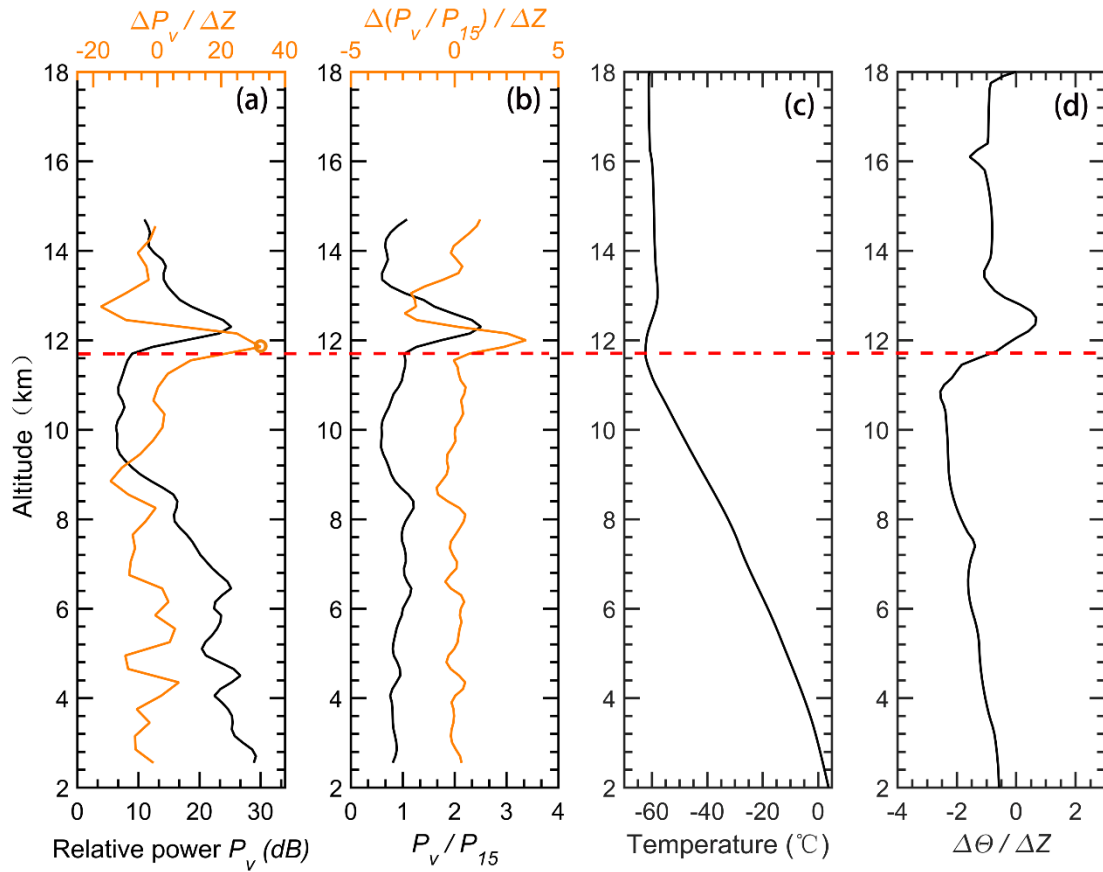
547

548 **Figures**



549

550 **Figure 1.** Distribution of the monthly total number of radar return echo power profiles  
551 that available from vertical beam in low mode, collected for the period November 2011-  
552 May 2017.

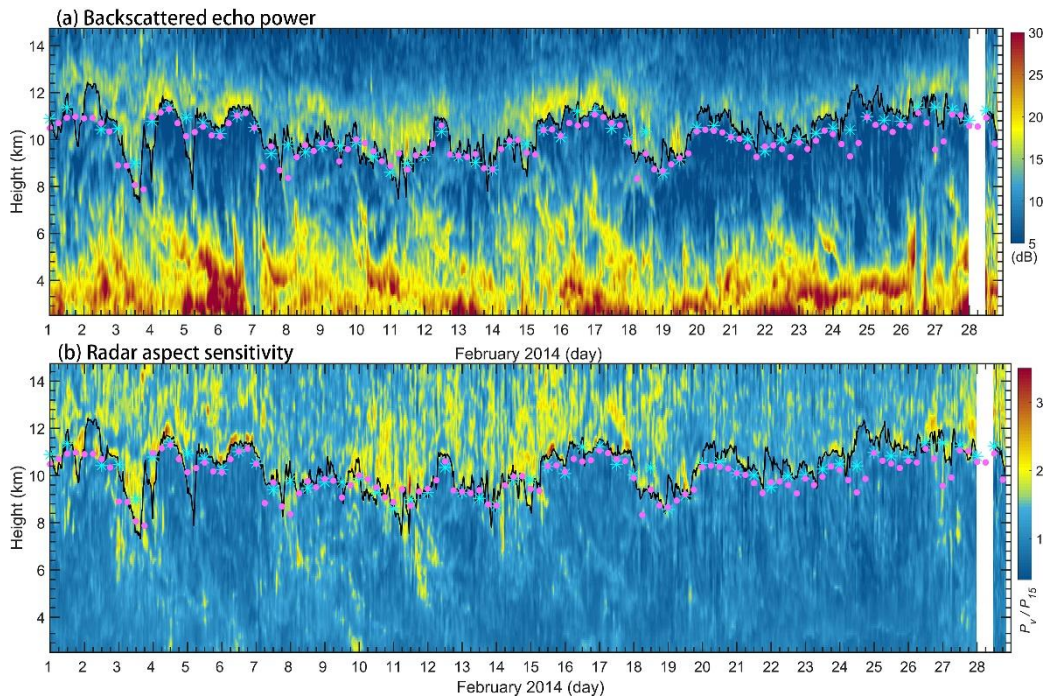


553

554 **Figure 2.** Example vertical profiles of (a) relative radar echo power (black line) along  
 555 with its gradient variation (orange line), (b) radar aspect sensitivity (black line) along  
 556 with its gradient variation (orange line), (c) radiosonde temperature and (d) potential  
 557 temperature gradient on 00 UT 04 November 2011. The horizontal red dashed line  
 558 marks the LRT height. The orange circle in Fig. 2a denotes the RT height.

559

560



561

562 **Figure 3.** Altitude-time intensity plot of (a) radar backscattered echo power and (b)

563 radar aspect sensitivity for February 2014. The tropopauses determined based on the

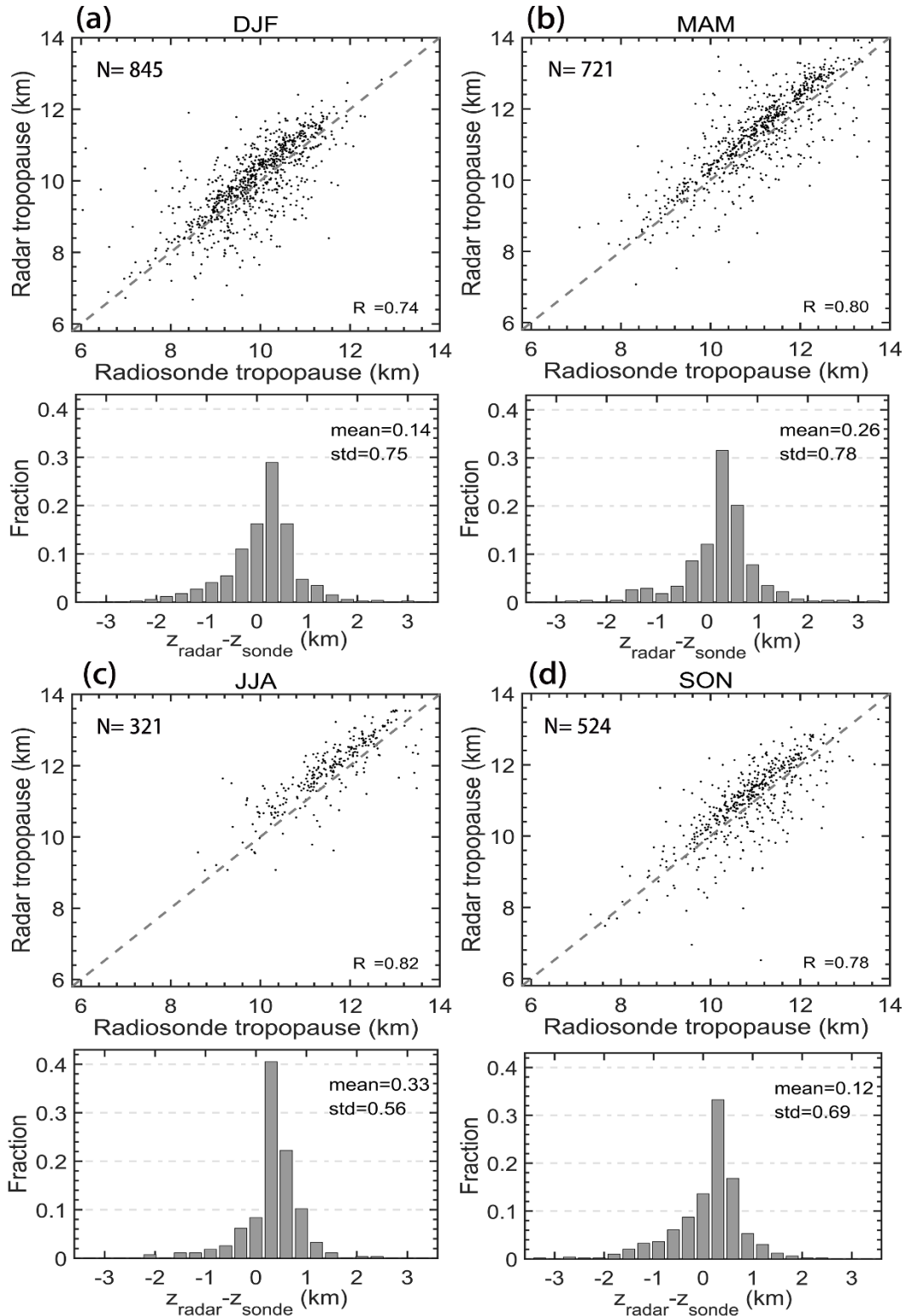
564 radar echo definition are shown as a black solid curve. The cyan asterisks ‘\*’ and pink

565 dots indicate the location of the LRT derived from simultaneous twice daily radiosonde

566 data and the PVT from ECMWF ERA-Interim reanalysis, respectively. White stripe

567 indicates the time frame of radar missing data.

568



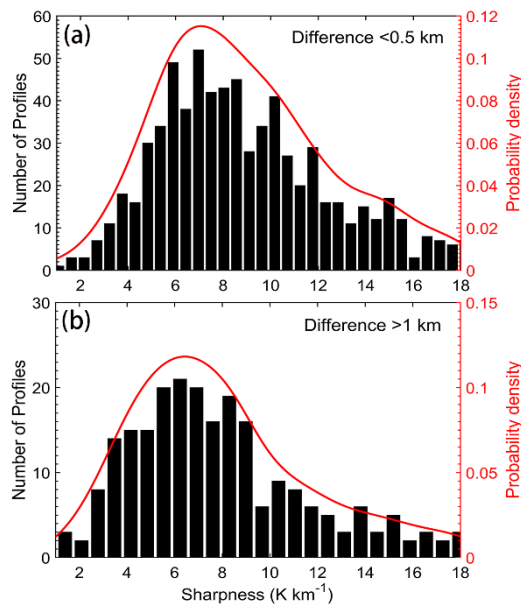
569

570 **Figure 4.** Seasonal scatterplots of the RT versus LRT and histogram distribution of  
 571 altitude differences between the RT and the LRT, for (a) winter DJF, (b) spring MAM,  
 572 (c) summer JJA, and (d) autumn SON, during the period November 2011-May 2017.

573 The positive values in the histogram indicate the RT locating at a higher level than the  
574 LRT. The grey dashed line shows the 1:1 line. Here, 'N', 'R<sup>2</sup>', 'mean', and 'std' indicate  
575 the sample numbers, correlation coefficient, mean difference, and standard deviation of  
576 the difference, respectively.

577

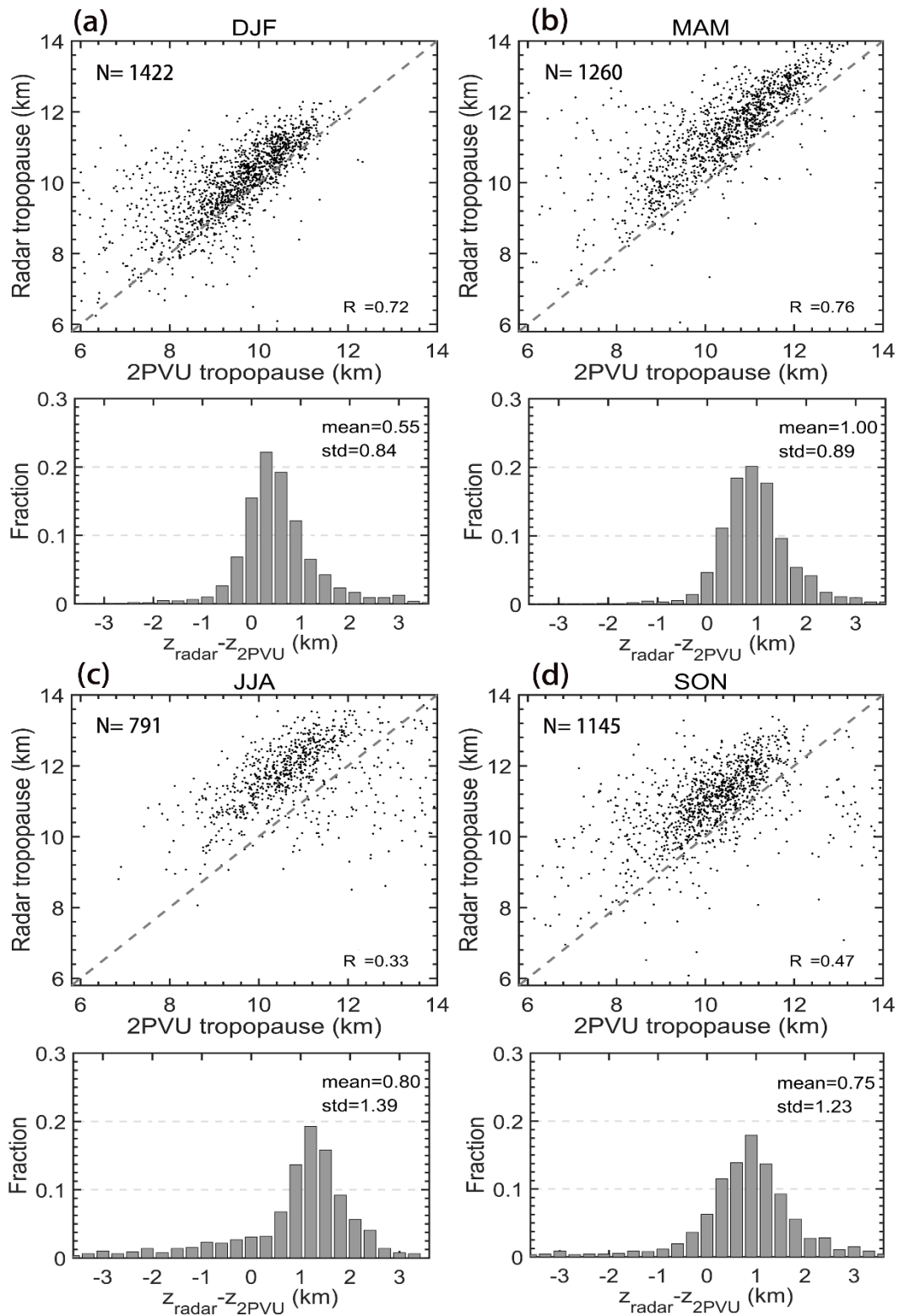
578



579

580 **Figure 5.** Histogram distribution of the tropopause sharpness for (a) difference < 0.5  
581 km, and (b) > 1 km respectively between the LRT and the RT.

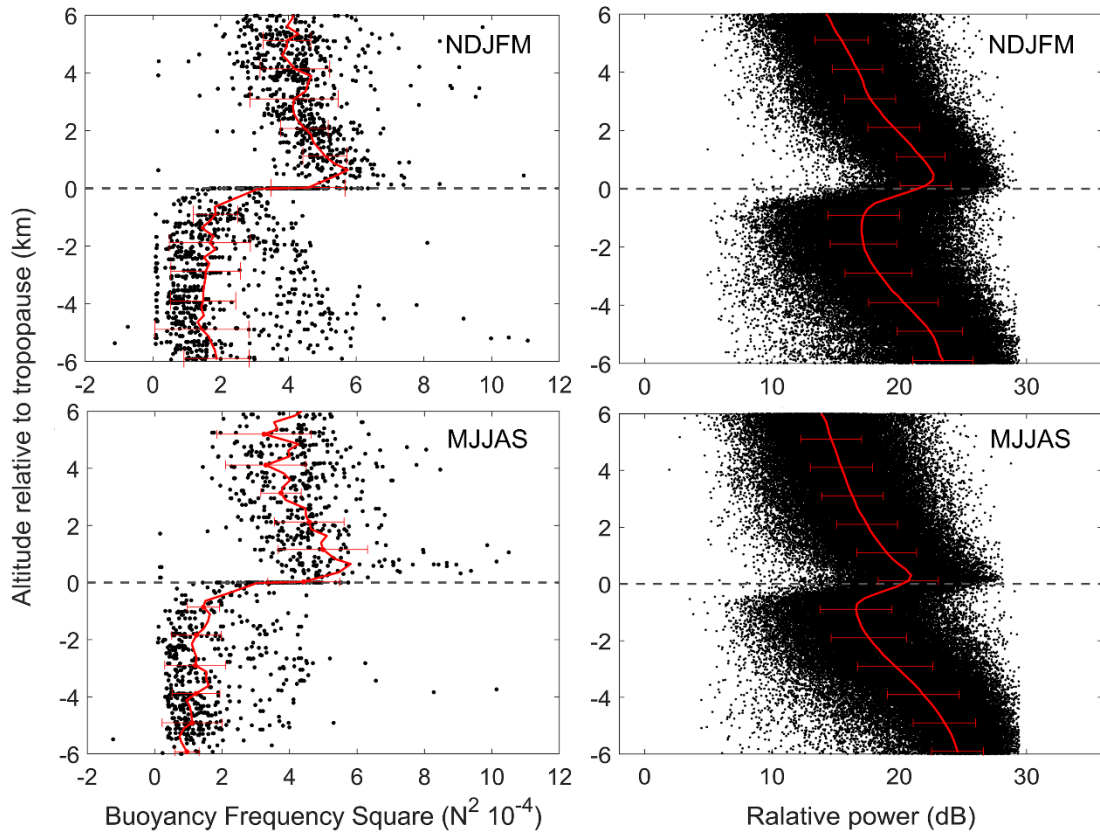
582



583

584 **Figure 6.** Same as figure 4, but for the comparison between the RT and the PVT.

585

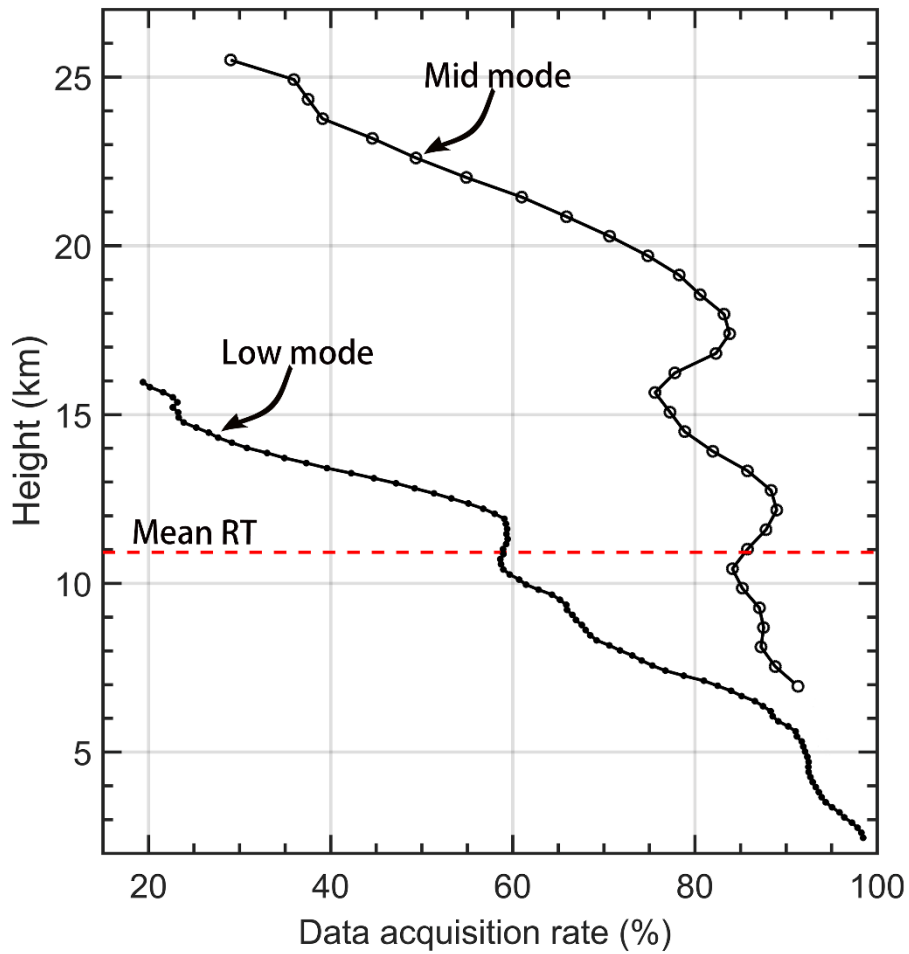


586

587 **Figure 7.** Scatterplots of (left panels) static stability ( $N^2$ ) and (right panels) radar  
 588 relative echo power as a function of altitude relative to the LRT (left panels) and RT  
 589 (right panels) for extended winter (NDJFM) and summer (MJJAS) seasons for two  
 590 specific years 2012-2013. Red lines in each panel denote the corresponding mean  
 591 profiles and the error bars indicate the standard deviations.

592

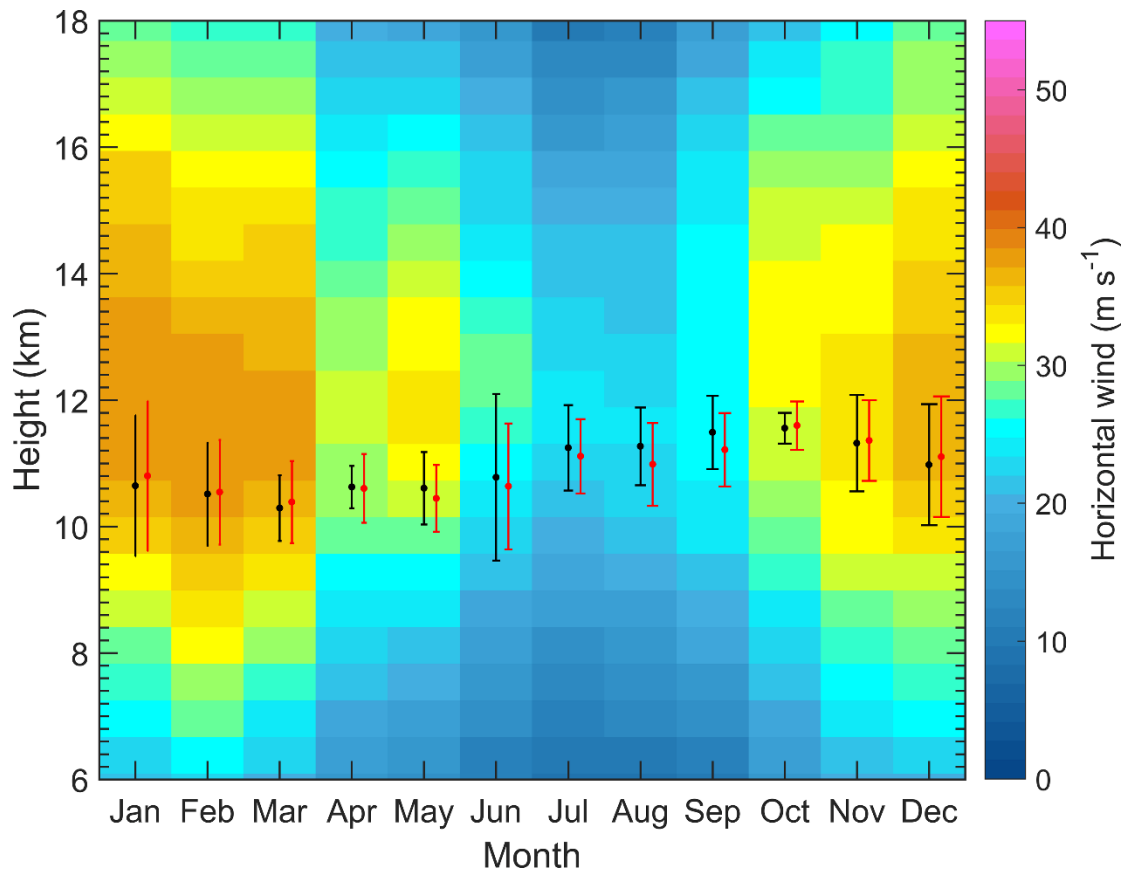
593



594

595 **Figure 8.** Vertical height profiles of the averaged effective radar wind data acquisition  
 596 rate in low mode and middle mode during November 2011-May 2017. The red dashed  
 597 line indicates the mean RT height.

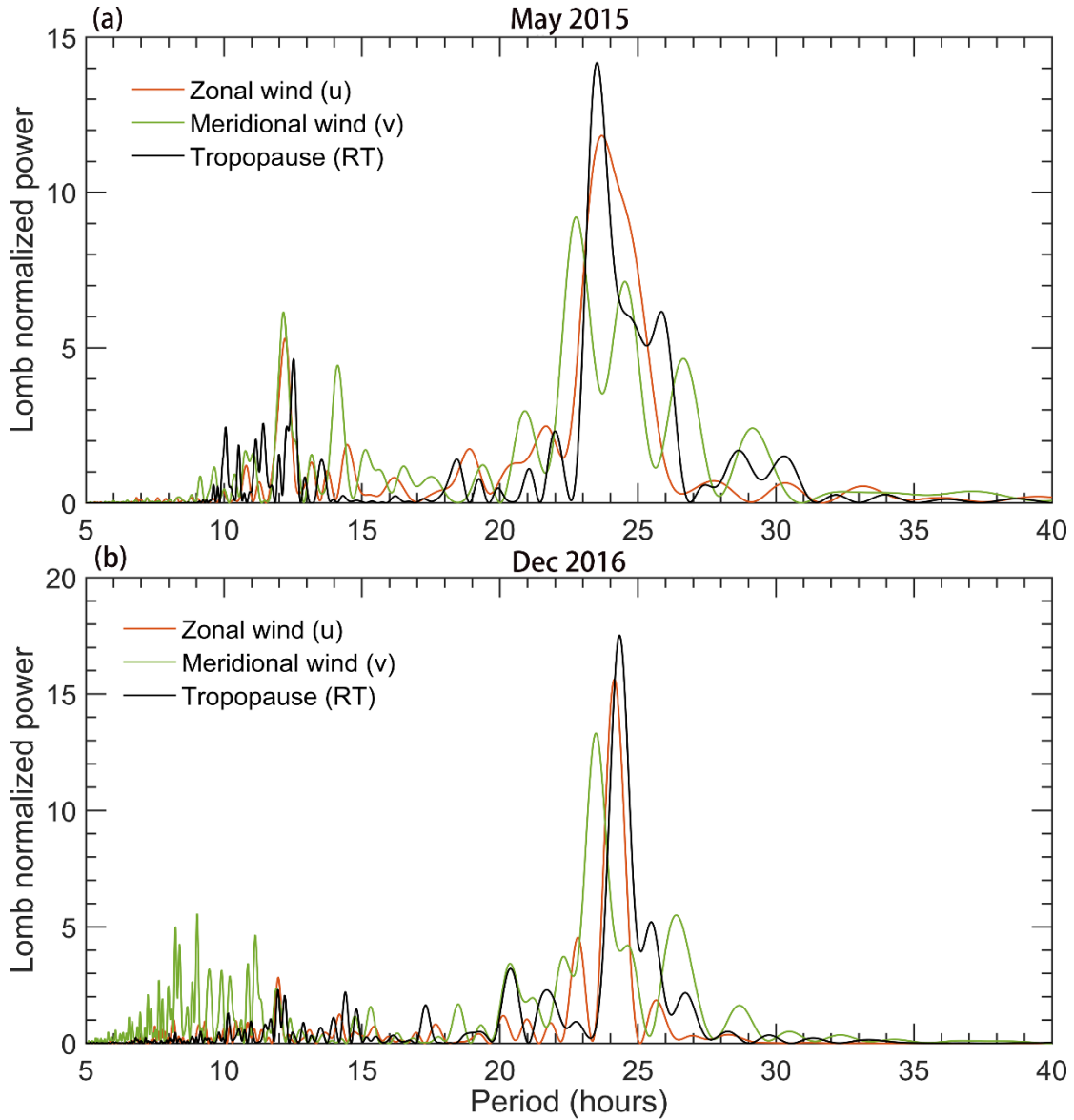
598



599

600 **Figure 9.** Height-time intensity map of monthly mean horizontal wind speed (shaded,  
 601 m/s) derived from the middle mode of Beijing MST radar, during November 2011-May  
 602 2017. Also shown is the monthly mean height of RT (black dots) and LRT (red dots,  
 603 offset by +6 days) along with the vertical error bars representing the standard deviations.

604



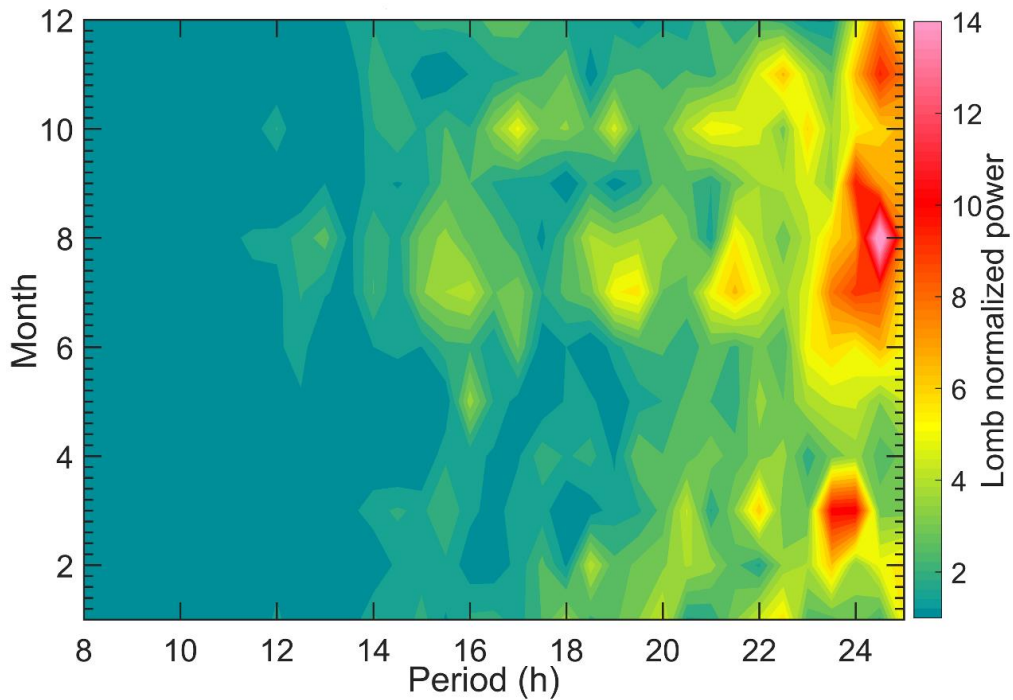
605

606 **Figure 10.** Lomb-Scargle periodograms of the RT height, zonal, and meridional wind

607 oscillations for specific months of (a) May 2015 and (b) December 2016. The zonal and

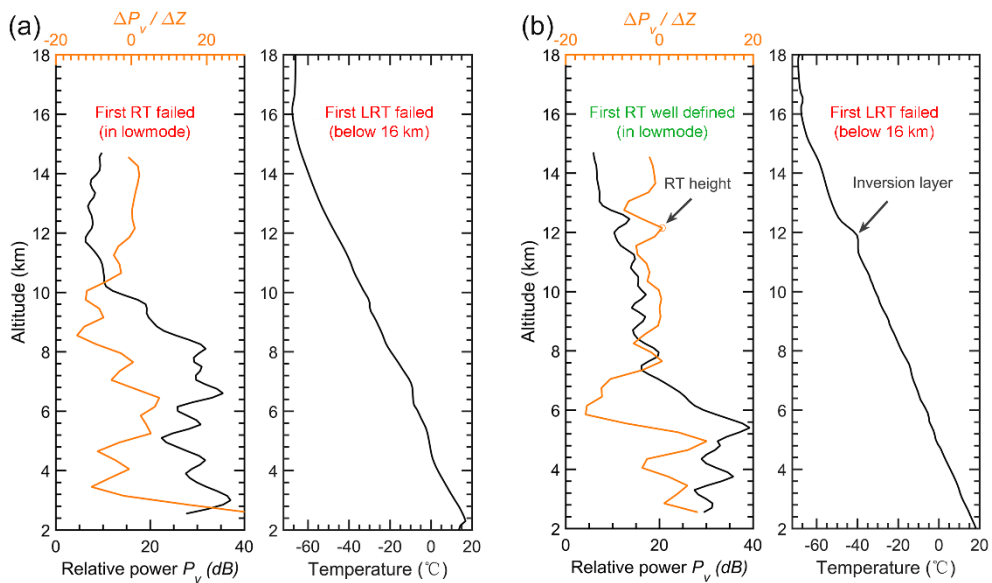
608 meridional wind for (a) is sampled at 9.85 km and (b) at 11 km.

609



610

611 **Figure 11.** Mean Lomb-Scargle periodograms of RT height as a function of the time of  
 612 month during November 2011-May 2017.



613

614 **Figure 12.** Example profiles of radar echo power and radiosonde temperature that (a)  
 615 both the RT and LRT definitions fail due to the continuing decrease in temperature on  
 616 00 UTC 7 July 2012 and (b) the temperature inversion layer failed to meet the LRT  
 617 definition but well defined in RT definition on 12 UTC 02 August 2012. Please note  
 618 that we only consider the conditions below 16 km.